

See discussions, stats, and author profiles for this publication at: <https://www.researchgate.net/publication/7768405>

Layering, condensation, and evaporation of short chains in narrow slit pores

ARTICLE *in* THE JOURNAL OF CHEMICAL PHYSICS · JULY 2005

Impact Factor: 2.95 · DOI: 10.1063/1.1924603 · Source: PubMed

CITATIONS

25

READS

8

3 AUTHORS, INCLUDING:



Jianzhong Wu

University of California, Riverside

155 PUBLICATIONS 4,318 CITATIONS

SEE PROFILE

Layering, condensation, and evaporation of short chains in narrow slit pores

Zhidong Li, Dapeng Cao, and Jianzhong Wu^{a)}

Department of Chemical and Environmental Engineering, University of California, Riverside, California 92521-0425

(Received 21 March 2005; accepted 5 April 2005; published online 10 June 2005)

The phase behavior of short-chain fluids in slit pores is investigated by using a nonlocal-density-functional theory that takes into account the effects of segment size, chain connectivity, and van der Waals attractions explicitly. The layering and capillary condensation/evaporation transitions are examined at different chain length, temperature, pore width, and surface energy. It is found that longer chains are more likely to show hysteresis loops and multilayer adsorptions along with the capillary condensation and evaporation. Decreasing temperature favors the inclusion of layering transitions into the condensation/evaporation hysteresis loops. For large pores, the surface energy has relatively small effect on the pressures of the capillary condensation and evaporation but affects significantly on the layering pressures. It is also observed that all phase transitions within the pore take place at pressures lower than the corresponding bulk saturation pressure. The critical temperature of condensation/evaporation is always smaller than that of the bulk fluid. All coexistence curves for confined phase transitions are contained within the corresponding bulk vapor-liquid coexistence curve. As in the bulk phase, the longer the chain length, the higher are the critical temperatures of phase transitions in the pore. © 2005 American Institute of Physics. [DOI: 10.1063/1.1924603]

I. INTRODUCTION

Adsorption and phase transitions of chainlike molecules in confined geometry are of fundamental importance in a number of industrial applications such as adhesion, lubrication, surface coating, and paint technologies.^{1,2} Fluids under confinement may exhibit structure and phase behavior significantly different from those in the bulk. For instance, chain molecules near a solid surface give rise to a number of intricate prewetting and wetting transitions that are entirely absent in the corresponding bulk fluids.^{3–5} The situation becomes even more complicated for polymeric fluids in micropores because some characteristic measures of confinement, e.g., pore size and geometry, also play a vital role. The interplay between fluid-surface and fluid-fluid interactions leads to diverse phase transitions including layering, condensation, evaporation, and surface freezing.^{6–11} Despite the significant conceptual and practical importance of confined polymeric fluids, molecular-level structural properties and phase transitions remain poorly understood. To some extent, this is due to both the lack of efficient experimental tools for studying phase transitions at small length scale and the dearth of rigorous theoretical approaches for realistic systems. The diversity of phase transitions in confined polymeric fluids also increases the cost and difficulty of numerical simulations dramatically.

In recent years, several versions of polymer density-functional theory have been proposed for representing the structure and thermodynamic properties of polymeric fluids

under inhomogeneous situations.^{12–16} At least for relatively simple models of polymeric systems, it has been demonstrated that the density-functional approach is able to quantitatively reproduce segment-level microscopic structures as well as thermodynamic potentials from molecular simulations at significantly less computational cost.^{16–21} With explicit consideration of surface and intermolecular interactions, the density-functional approach thus provides a new avenue to explore the rich equilibrium behavior of confined polymeric systems.^{9,11} In this work, we investigate the scope of a recently developed nonlocal-density-functional theory for representing layering transitions, capillary condensation, and evaporation of short-chain fluids in slitlike pores. The theoretical results are expected to provide insights on the interplay of rich phase transitions in confined polymeric systems.

II. THEORY

We consider short Lennard-Jones (LJ) chains confined between two parallel smooth surfaces in equilibrium with a bulk vapor phase. The system resembles the confinement of normal alkanes between two mica surfaces as recently investigated using surface-force apparatus (SFA).^{3,22} Each molecule consists of identical beads that are freely jointed into a linear chain with the bond length identical to the size parameter (σ) of the LJ potential. For direct comparison with simulation results, the intersegment potential is truncated at the cutoff distance $r_c = 2.5\sigma$. As originally introduced in the Baker-Henderson perturbation theory, the LJ potential between segments is divided into a short-ranged repulsion and a longer-ranged attraction in all theoretical calculations per-

^{a)}Author to whom correspondence should be addressed. Electronic mail: jwu@engr.ucr.edu

formed in this work. The repulsive part is further approximated by an effective hard-sphere potential with the diameter²³

$$d = \frac{1 + 0.2977T^*}{1 + 0.33163T^* + 0.00104771T^{*2}}\sigma, \quad (1)$$

where $T^* = k_B T / \varepsilon$ is the reduced temperature with k_B being the Boltzmann constant and T being the absolute temperature.

The interaction between a segment and each surface of the slit pore is represented by the Steele's 10-4-3 potential,²⁴

$$V_s(z) = \varepsilon_w \left[\frac{2}{5} \left(\frac{\sigma_w}{z} \right)^{10} - \left(\frac{\sigma_w}{z} \right)^4 - \frac{\sigma_w^4}{3\Delta(z + 0.61\Delta)^3} \right], \quad (2)$$

where z is the perpendicular distance from the surface. As in our previous work,²⁵ the parameters of the wall potential are given by

$$\sigma_w = \sigma, \quad \varepsilon_w = \lambda \varepsilon, \quad \Delta = 0.7071\sigma. \quad (3)$$

For chain molecules in a slit pore, the total external potential for each segment is equal to the summation of that from individual walls,

$$\nu(z) = V_s(z) + V_s(H - z), \quad (4)$$

where H stands for the pore width.

In a previous work,²⁰ we reported an expression for the Helmholtz energy functional of freely jointed tangent LJ chains that is derived from a modified fundamental measure theory (MFMT) for short-ranged repulsion and the direct correlation function (DCF) of monomeric bulk fluids for the longer-ranged van der Waals attraction. The effect of chain connectivity on the intramolecular correlations is taken into account by extending the first-order thermodynamic perturbation theory (TPT1) to inhomogeneous polymeric fluids.¹⁶ The numerical performance of the Helmholtz energy functional was tested by extensive comparison with Monte Carlo simulation results for the segment-level-density profiles and the correlation functions of Lennard-Jones chains in slit pores, near isolated nanoparticles and in the bulk.²⁰

Briefly, the intrinsic Helmholtz energy functional F is decomposed into four contributions,

$$F = F^{\text{id}}[\rho_M(\mathbf{R})] + F_{\text{hs}}^{\text{ex}}[\rho(\mathbf{r})] + F_{\text{ch}}^{\text{ex}}[\rho(\mathbf{r})] + F_{\text{att}}^{\text{ex}}[\rho(\mathbf{r})]. \quad (5)$$

Here $\mathbf{R} \equiv (\mathbf{r}_1, \mathbf{r}_2, \dots, \mathbf{r}_M)$ stands for a set of coordinates describing the positions of M segments in each chain, and $\rho(\mathbf{r})$ represents the overall segment density profile. The subscripts hs, ch, and att denote, respectively, contributions to the excess Helmholtz energy functional due to the short-ranged repulsion, chain connectivity, and longer-ranged van der Waals attractions. The ideal-gas part of the Helmholtz energy functional $F^{\text{id}}[\rho_M(\mathbf{R})]$ is known exactly

$$\beta F^{\text{id}} = \int d\mathbf{R} \rho_M(\mathbf{R}) [\ln \rho_M(\mathbf{R}) - 1] + \beta \int d\mathbf{R} \rho_M(\mathbf{R}) V_b(\mathbf{R}), \quad (6)$$

where $V_b(\mathbf{R})$ represents the bonding potential. For a freely jointed tangent chain, $V_b(\mathbf{R})$ is given by

$$\exp[-\beta V_b(\mathbf{R})] = \prod_{i=1}^{M-1} \frac{\delta(|\mathbf{r}_{i+1} - \mathbf{r}_i| - \sigma)}{4\pi\sigma^2}, \quad (7)$$

where $\delta(r)$ stands for the Dirac-delta function and $\beta = 1/k_B T$.

The excess Helmholtz energy functional due to the effective hard-sphere repulsion is represented by a MFMT (Refs. 26 and 27),

$$\beta F_{\text{hs}}^{\text{ex}} = \int d\mathbf{r} \Phi^{\text{hs}}[n_\alpha(\mathbf{r})], \quad (8)$$

where

$$\begin{aligned} \Phi^{\text{hs}} = & -n_0 \ln(1 - n_3) + \frac{n_1 n_2 - \mathbf{n}_{v1} \mathbf{n}_{v2}}{1 - n_3} \\ & + \frac{1}{36\pi} \left[n_3 \ln(1 - n_3) + \frac{n_3^2}{(1 - n_3)^2} \right] \\ & \times \frac{(n_2^3 - 3n_2 \mathbf{n}_{v2} \mathbf{n}_{v2})}{n_3^3}, \end{aligned} \quad (9)$$

and the expressions for the weighted densities,

$$n_\alpha(\mathbf{r}) = \int \rho(\mathbf{r}') \omega^{(\alpha)}(|\mathbf{r} - \mathbf{r}'|) d\mathbf{r}', \quad (10)$$

can be found in Rosenfeld's original work.²⁸ Here the effective hard-sphere diameter d instead of the LJ diameter σ should be used for calculating the weighted densities.

The third term on the right-hand side of Eq. (5) arises from the effect of chain connectivity on the intramolecular correlations. According to a semiempirical extension of the first-order thermodynamic perturbation theory,¹⁶ this part of the excess Helmholtz energy functional can be approximated as

$$\beta F_{\text{ch}}^{\text{ex}} = \frac{1 - M}{M} \int d\mathbf{r} n_0 \zeta \ln y(n_3), \quad (11)$$

where $\zeta = 1 - \mathbf{n}_{v2} \mathbf{n}_{v2} / n_2^2$ represents an inhomogeneity factor and the cavity correlation function (CCF) is given by

$$y(n_3) = 1 + \sum_{i,j=1}^5 a_{ij}(n_3)^i \left(\frac{6\sigma^3}{\pi d^3} \right)^i (T^*)^{1-j}. \quad (12)$$

The density-independent parameters used in Eq. (12) a_{ij} can be found from Monte Carlo simulations.²⁹

Finally, the attractive part of the excess Helmholtz energy functional $F_{\text{att}}^{\text{ex}}[\rho(\mathbf{r})]$ is approximated by a functional Taylor expansion,

$$\beta F_{\text{att}}^{\text{ex}} = -\frac{1}{2} \int \int d\mathbf{r} d\mathbf{r}' C^{\text{att}}(|\mathbf{r} - \mathbf{r}'|) \rho(\mathbf{r}) \rho(\mathbf{r}'). \quad (13)$$

Here the direct correlation function, $C^{\text{att}}(r)$, is obtained from the mean-spherical approximation (MSA) for the corresponding monomeric fluid in the bulk.^{20,30}

In the bulk limit, Eq. (5) is essentially the same as the Helmholtz energy from the statistical associating fluid theory (SAFT).³¹ In this case, the equation of state is given by

$$P^* = \rho_b^* T^* \left\{ \frac{1 + \eta + \eta^2 - \eta^3}{(1 - \eta)^3} - 2\pi\rho_b \int C^{\text{att}}(r)r^2 dr + \frac{1 - M}{M} \left(1 + \rho_b \frac{\partial \ln y_b}{\partial \rho_b} \right) \right\}, \quad (14)$$

where the reduced pressure is defined as $P^* = P\sigma^3/\varepsilon$, the reduced segment bulk density is $\rho_b^* = \rho_b\sigma^3$, and the packing fraction is $\eta = \pi/6\rho_b d^3$ with ρ_b being the segment bulk density. Equation (14) provides a connection between the chemical potential used in density-functional theory (DFT) calculations and the bulk polymer density. In addition, it allows us to calculate the saturation pressure at a given temperature following standard vapor-liquid equilibrium calculations.³²

The equilibrium configuration of polymer chains satisfies the Euler-Lagrange equation,

$$\rho_M(\mathbf{R}) = \exp[\beta\mu_M - \beta V_b(\mathbf{R}) - \beta V_M(\mathbf{R}) - \beta\Lambda(\mathbf{R})], \quad (15)$$

where $V_M(\mathbf{R})$ is the external potential per molecule and $\Lambda(\mathbf{R}) = \delta F^{\text{ex}}/\delta\rho_M(\mathbf{R})$ is an effective potential field due to all nonbonded intra- and intermolecular interactions. Because the excess Helmholtz energy functional depends only on the segment density, the effective self-consistent molecular potential can be written as

$$\Lambda(\mathbf{R}) = \frac{\delta F^{\text{ex}}}{\delta\rho_M(\mathbf{R})} = \sum_{i=1}^M \frac{\delta F^{\text{ex}}}{\delta\rho(\mathbf{r}_i)}. \quad (16)$$

Substituting Eq. (16) into Eq. (15) yields

$$\rho_M(\mathbf{R}) = \exp \left\{ \beta\mu_M - \beta V_b(\mathbf{R}) - \beta \sum_{i=1}^M \lambda(\mathbf{r}_i) \right\}, \quad (17)$$

with

$$\lambda(\mathbf{r}_i) = \frac{\delta F^{\text{ex}}}{\delta\rho(\mathbf{r}_i)} + \nu(\mathbf{r}_i), \quad (18)$$

where $\nu(\mathbf{r}_i)$ represents the external potential energy on individual segments. The individual segment density $\rho_{\text{si}}(\mathbf{r})$ can be calculated from

$$\rho_{\text{si}}(\mathbf{r}) = \int d\mathbf{R} \delta(\mathbf{r} - \mathbf{r}_i) \exp \left[\beta\mu_M - \beta V_b(\mathbf{R}) - \beta \sum_{j=1}^M \lambda(\mathbf{r}_j) \right], \quad (19)$$

and the overall segment density is equal to the summation of the densities for all segments

$$\rho(\mathbf{r}) = \exp(\beta\mu_M) \int d\mathbf{R} \sum_{i=1}^M \delta(\mathbf{r} - \mathbf{r}_i) \times \exp[-\beta V_b(\mathbf{R}) - \beta \sum_{j=1}^M \lambda(\mathbf{r}_j)]. \quad (20)$$

Equations (19) and (20) are solved via the Picard iteration method.³⁰ Once we have the equilibrium density profile, we can subsequently calculate the total amount of adsorption and thermodynamic variables at a given polymer chemical potential or equivalently, the bulk polymer density.

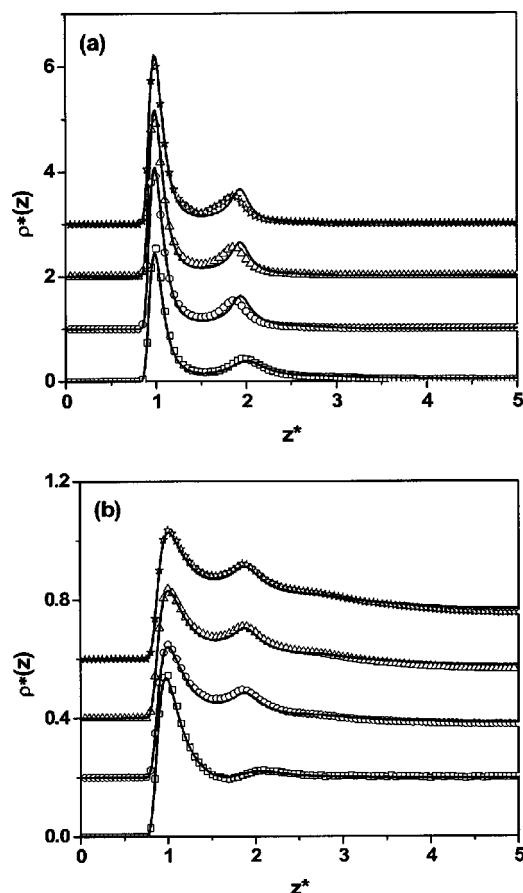


FIG. 1. Segment density profiles for LJ chains with $M=1, 4, 8$, and 16 in an attractive slit pore at $H^*=10.0$ and $\lambda=6.283$. Here the average packing fraction is $\eta_{\text{av}}=0.1$ and the reduced temperatures are (a) $T^*=1.0$ and (b) $T^*=4.0$. The symbols and lines represent simulation and DFT results, respectively. For clarity, the density profiles for $M=4, 8$, and 16 have been shifted upward consecutively by 1.0 for $T^*=1.0$ and by 0.2 for $T^*=4.0$.

III. RESULTS AND DISCUSSION

We consider first the distributions of chain molecules in an attractive slit pore. To test the theoretical predictions, we run in parallel configurational bias Monte Carlo (CBMC) simulations in the canonical ensemble where the number of particles, temperature, and confining volume are fixed. For direct comparison with theory and simulation results, the chemical potential in the DFT calculations is adjusted such that the two approaches yield the same average segment density in the pore.

Figure 1 presents the density profiles of LJ 16mers, 8mers, and 4mers near one surface of the slit pore at two different reduced temperatures ($T^*=1.0$ and 4.0). For comparison, the density profiles of the corresponding monomeric fluid are also included. For all cases the average packing fraction inside the slit pore is $\eta_{\text{av}}=0.1$ and the reduced pore width is $H^*=10.0$. The agreement between theory and simulation is nearly perfect. At low temperature ($T^*=1.0$), the first-peak density slightly increases with the chain length due to the subtle interplay of surface energy, the translational entropy related to the center of mass, and configurational chain entropy. We notice that for hard-sphere chains in a hard split pore (athermal), the contact density of polymeric segments is lower than that of monomers of the same packing

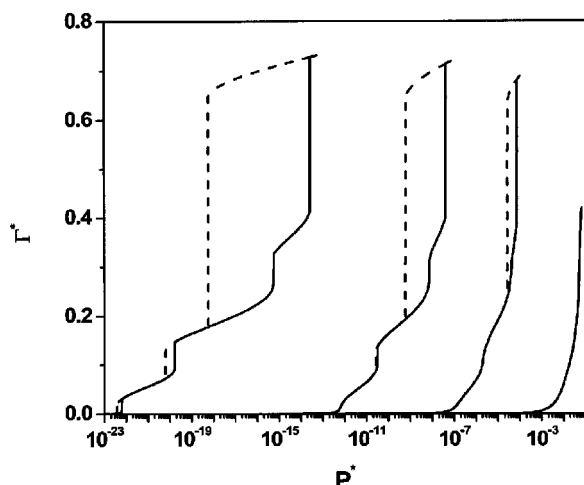


FIG. 2. Adsorption isotherms of LJ chains in a slit pore at $T^*=1.0$, $H^*=10.0$, and $\lambda=6.283$ for $M=1, 4, 8$, and 16 (from right to left). The solid and dashed lines represent adsorption and desorption processes, respectively.

density. In other words, regarding the effect of chain length on surface selectivity the trends can be completely opposite, depending on the properties of polymers and polymer-wall interactions. The observation for athermal systems is partially reflected as the temperature increases. At high temperature [Fig. 1(b), $T^*=4.0$], the first-peak segment density of the monomer fluid is higher than that of those consisting of chain molecules at the same average packing density. Interesting enough, the decline of the first-peak density for longer chain molecules is partially compensated by an enhancement of the nearby second peak (shoulder). Such structure is completely missing in the corresponding monomeric system.

Figure 2 depicts the adsorption/desorption isotherms of 16mers, 8mers, 4mers, and monomers at $T^*=1.0$. The reduced excess adsorption is defined as

$$\Gamma^* = \frac{1}{H} \int_0^H dz [\rho(z) - \rho_b] \sigma^3. \quad (21)$$

Here the reduced pore width is $H^*=H/\sigma=10.0$ and the surface energy parameter is $\lambda=6.283$. For the monomeric system, the amount of adsorption rises smoothly with the bulk pressure. Because the temperature we considered here is higher than the critical point of the monomeric fluid ($T^*=0.95$), no capillary condensation is observed. For Lennard-Jones chains, however, the adsorption isotherms entail a number of layering transitions and the difference in the adsorption and desorption isotherms gives rise to the hysteresis loops. As expected, the layering transitions become more distinct and occur at lower pressure as the chain length increases. However, the total amount of adsorption after capillary condensation is essentially independent of the chain length. The situation can be different as the pore width is comparable to the range of surface attraction. In that case, the surface energy affects both layering and capillary condensation directly. Both adsorption and desorption processes exhibit a layering behavior but in general layering transitions in the desorption process are less likely in comparison with the adsorption process.

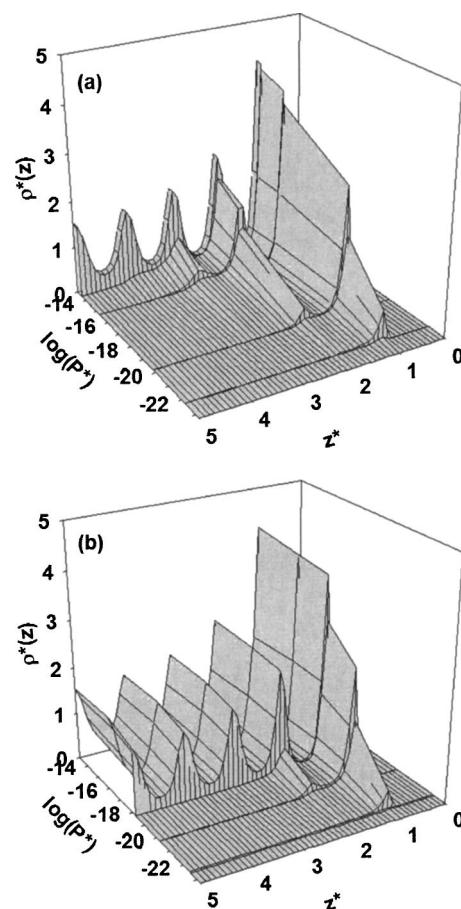


FIG. 3. Average segment density profiles of LJ chains at $T^*=1.0$, $H^*=10.0$, $M=16$, and $\lambda=6.283$ for (a) adsorption and (b) desorption.

The layering and condensation/evaporation transitions are easily identifiable from the variation of density profiles with the bulk vapor pressure as depicted in Fig. 3 for 16mers at $T^*=1.0$, $H^*=10.0$, and $\lambda=6.283$. Figure 3(a) shows that as the pressure increases, three adsorption layers appear consecutively in the pore and a liquid-like structure is developed after the capillary condensation. During the desorption process, as shown in Fig. 3(b), the capillary evaporation takes place at a pressure much lower than the condensation pressure.

The phase transitions of a polymeric fluid near an attractive surface are extremely sensitive to temperature. Figure 4 shows the adsorption/desorption isotherms for Lennard-Jones 8mers at different values of the reduced temperature. At low temperature ($T^*=0.7$), the adsorption isotherm exhibits multiple layering transitions before the complete filling. Here all layering transitions are metastable because they are completely contained within the hysteresis loops. As the temperature increases, the layering transitions are consecutively shifted out of the hysteresis loops and the jumps in the adsorption isotherm become more continuous. At $T^*=1.4$, the layering transitions disappear entirely and the adsorption isotherm exhibits a continuous pore filling step before the capillary condensation. With the further increase in temperature, the fading hysteresis loop shifts toward higher pressure and vanishes completely when the temperature is above a critical value ($T^*=1.8$). We notice that as the reduced temperature

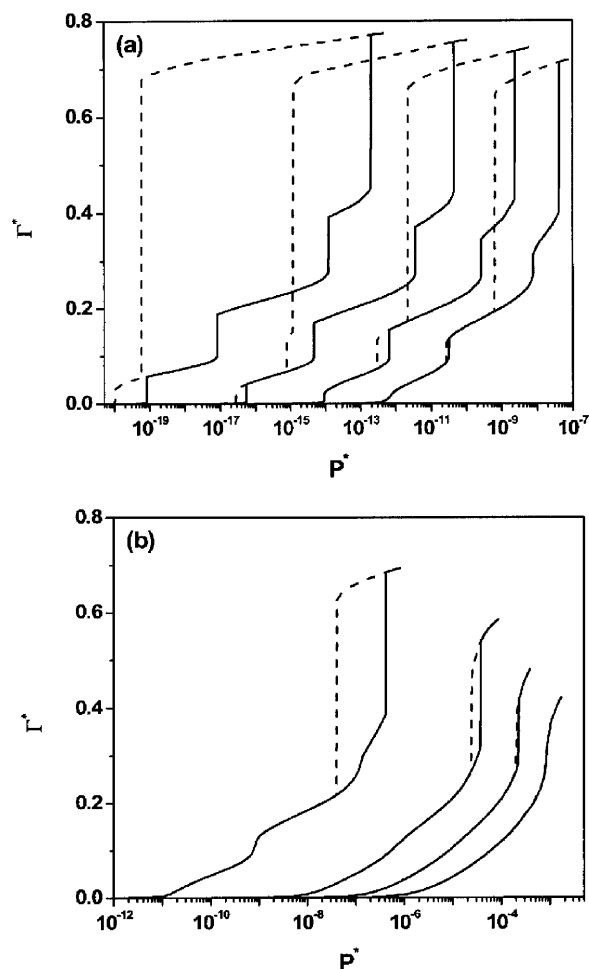


FIG. 4. Adsorption isotherms at $H^* = 10.0$, $\lambda = 6.283$, and $M = 8$ for (a) $T^* = 0.7, 0.8, 0.9$, and 1.0 ; (b) $T^* = 1.1, 1.4, 1.6$, and 1.8 . The sequence is from left to right.

varies from 0.7 to 1.8, the pressure relevant to all the phase transitions spans over more than 15 orders of magnitude.

Figure 5 depicts the effect of pore size H^* on the adsorption behavior for 16mers at $T^* = 1.0$ and $\lambda = 6.283$. When the pore is sufficiently narrow ($H^* = 4.0$), the layering transitions are depressed but significant hysteresis remains between the adsorption and desorption processes. As the pore width increases, more and more layering transitions arise and some gradually shift outside of the hysteresis loop. Evidently, both the adsorption and desorption isotherms are highly sensitive to the pore width. As the size of the slit pore changes from $H^* = 4.0$ to 10.0, the condensation pressure changes over nearly ten orders of magnitude.

The adsorption of chain molecules in a slit pore is also highly sensitive to the surface energy. To explore this effect, we present in Fig. 6 the adsorption isotherms of LJ chains at different surface energies for 8mers at $T^* = 1.0$ and $H^* = 10.0$. The stronger surface energy, i.e., the larger λ value, the more probable are the layering transitions at the wall. At moderately attractive surface, layering transition becomes less probable. For chain molecules in a slit pore with strongly attractive walls ($\lambda = 10.283$), the major hysteresis loop lies outside of the layering transitions occurring at very low pressure. In comparison with layering transitions at low

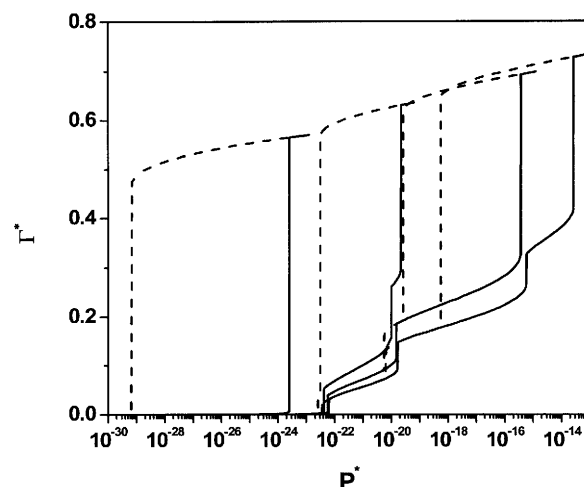


FIG. 5. Adsorption isotherms at $T^* = 1.0$, $\lambda = 6.283$, and $M = 16$ for $H^* = 4.0, 6.0, 8.0$, and 10.0 (from left to right).

temperature, the jumps in the layering transitions near a strongly attractive surface are recognizable but rather blurry. With the decrease of λ , the pressures corresponding to layering transitions and capillary condensation increase. Concurrently, the layer jumps become steeper and consecutively merge into the hysteresis loop. When the surface energy decreases to $\lambda = 4.283$, all the layers are contained inside the hysteresis loop and completely disappear at $\lambda = 2.283$. For large pores the surface energy has relatively small effect on the pressures of capillary condensation and evaporation but affects significantly on the pressures of layering transitions. As the λ changes from 10.283 to 2.283, the pressure spans nearly 16 orders of magnitude for layering transitions, but only three orders of magnitude for capillary condensation and one order of magnitude for capillary evaporation.

Based on the adsorption/desorption isotherms discussed above, we are able to construct the phase diagrams for the layering and condensation/evaporation transitions in slit pores. As a reference, we also calculate the saturation pressures and the vapor-liquid coexistence curves for the corresponding bulk fluids using the equation of state given in Eq. (14). Figures 7 and 8 show the phase diagrams of confined and bulk LJ chains of 4mers, 8mers, and 16mers in the $P^* - T^*$ and $\rho^* - T^*$ planes at $H^* = 10.0$ and $\lambda = 6.283$. The phase diagram for confined chains includes three consecutive layering transitions and the capillary condensation/evaporation. We observe that all phase transitions within the pore take place at pressures lower than the bulk saturation pressure. The confinement depresses the critical condensation/evaporation temperature, which is always smaller than the critical temperature of the bulk fluid. In addition, we find that for the conditions shown in Figs. 7 and 8, all coexistence curves for the confined phase transitions are contained within the corresponding bulk vapor-liquid coexistence curve (Fig. 8). As a result, the average coexistence densities in the pore are always smaller than the saturated liquid density in the bulk. The longer the chain length, the higher are the critical temperatures of layering transition, capillary condensation/evaporation, and bulk vapor-liquid equilibrium. For all the chain lengths considered here, the third layering transition is

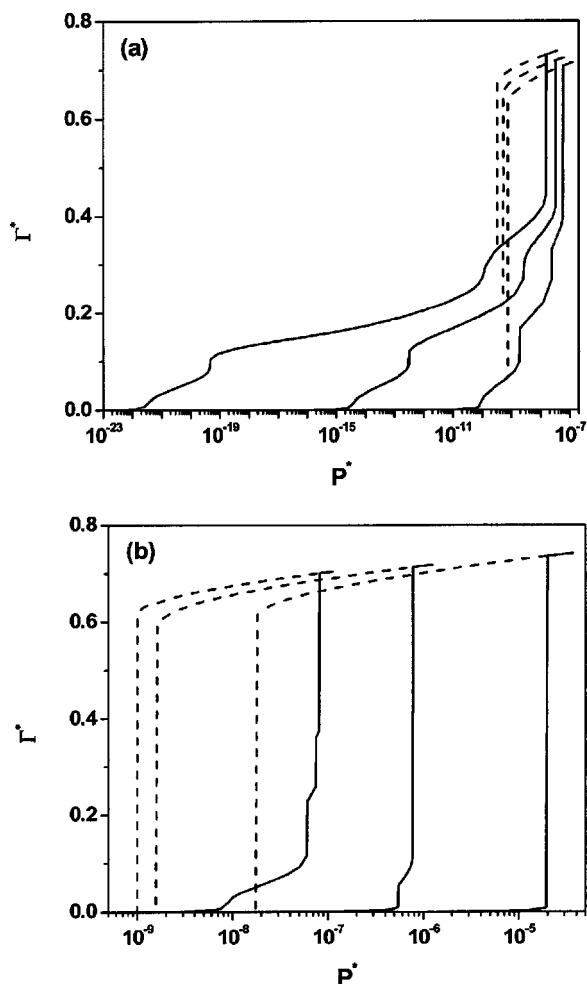


FIG. 6. Adsorption isotherms at $T^*=1.0$, $H^*=10.0$, and $M=8$ for (a) $\lambda = 10.283, 7.283$, and 5.283 ; (b) $\lambda = 4.283, 3.283$, and 2.283 . The sequence is from left to right.

always located within the evaporation coexistence curves. Therefore, it does not show up during the desorption process. At a lower temperature, the first and the second layer are also likely to be contained within the evaporation coexistence curves but this becomes more so as the chain length increases. The phase diagrams shown in Figs. 7 and 8 provide direct insights on the interplay among a number of phase transitions occurred in confined polymeric systems.

We should point out that the layering transitions and evaporation/condensation as shown in Figs. 7 and 8 are not truly at thermodynamic equilibrium. Indeed, these phase transitions reflect merely the metastable phase transitions as often observed in adsorption/desorption experiments. An important advantage of DFT is that it is relatively easy to calculate the grand potentials of the coexistence phases and thus determine the thermal equilibrium, i.e., the true phase equilibrium. Figure 9 shows as an example the thermodynamic equilibrium states of confined LJ 16mers at $T^*=0.9$, $H^*=10.0$, and $\lambda=6.283$ along with the adsorption/desorption isotherms that exhibit multiple layering transitions. From Fig. 9(b), each metastable phase transition is manifested as a distinctive drop in the reduced grand potential along the adsorption/desorption lines while the true thermodynamic equilibrium occurs only when the adsorption/desorption

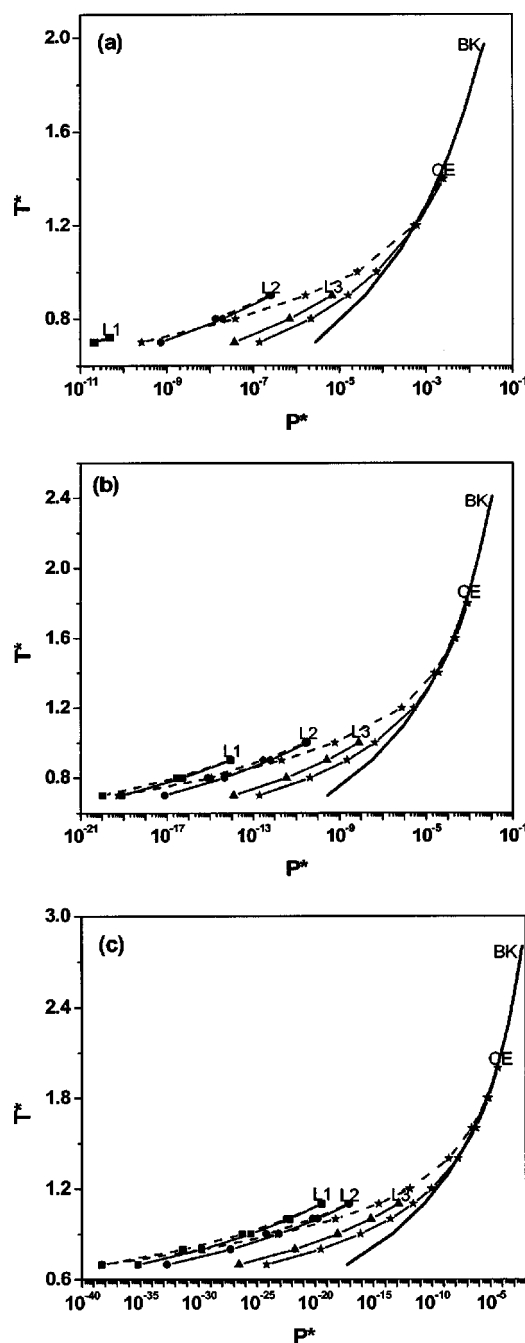


FIG. 7. Phase transitions of confined LJ chains at $H^*=10.0$ and $\lambda=6.283$ in the P^*-T^* diagram for (a) $M=4$, (b) $M=8$, and (c) $M=16$. The lines with squares, circles, triangles, and stars represent the first (L1), the second (L2), the third (L3) layering transitions, and the capillary condensation/evaporation (CE) transitions, respectively. The solid and dashed lines are for adsorption and desorption processes, respectively. The dark solid line makes the reduced saturation pressure of bulk (BK).

grand potentials come across. In the adsorption process, the grand potential monotonically decreases accompanied by three small and one big downward jumps corresponding to the three layering transitions and the capillary condensation, respectively. In the desorption process, conversely, the grand potential increases but also jumps downward in three steps at the pressures corresponding to the evaporation and two layering transitions. The three crossover points during the adsorption and desorption processes correspond to equilibrium phase transitions as marked by the thick solid lines in

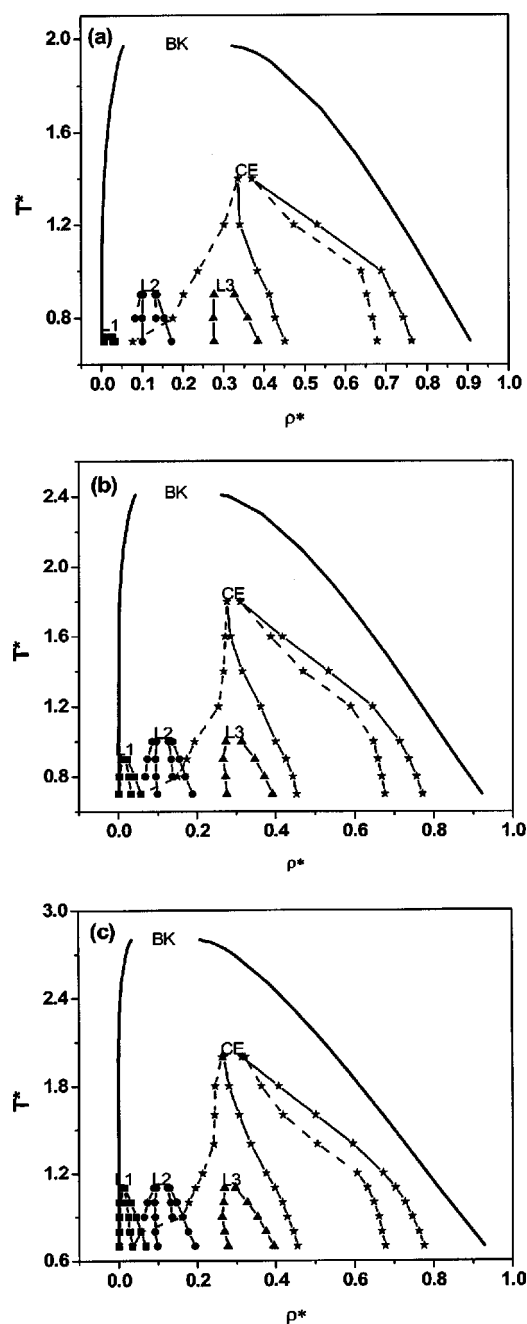


FIG. 8. The same as in Fig. 7 but in the ρ^*-T^* diagram. The dark solid lines mark the corresponding bulk gas-liquid coexistence curves.

Fig. 9(a). Although the coexistence equilibrium phases have the same grand potential, the total amounts of adsorption are in general very different.

IV. CONCLUSIONS

We have investigated the effect of the chain length, temperature, pore size, and surface energy on the adsorption behavior and phase transitions of LJ chains confined in slit pores. It is found that the fluid consisting of longer chain molecules is more likely to exhibit strong and metastable layering transitions. At low temperature, one or more layers are contained in the hysteresis loop. As the temperature increases, the layers are consecutively released from the hysteresis loop but the features of first-order phase transition are

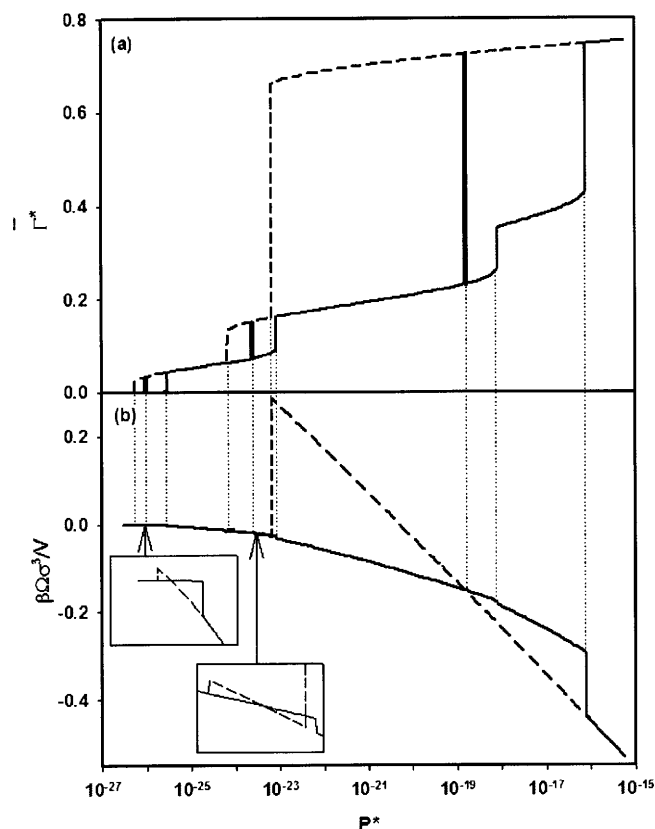


FIG. 9. (a) Adsorption isotherm and (b) reduced grand potential density at $T^*=0.9$, $H^*=10.0$, $M=16$, and $\lambda=6.283$. The dark solid lines in (a) mark the equilibrium transitions.

weakened and the metastability gradually vanishes. The width of the hysteresis loop decreases and eventually disappears with the increase of temperature. The pore size also plays an important role in the determination of the shape of adsorption isotherms. For sufficiently narrow pores, the layering transitions disappear completely and only capillary condensation occurs. As the pore width increases, more and more adsorption layers arise. By increasing the surface energy, the hysteresis loop becomes narrower and all the layers appear outside the hysteresis loop with weakened intensity. Upon reducing the surface energy, the hysteresis loop becomes wider and finally all the layering transitions disappear.

In addition to the adsorption/desorption isotherms, we have also examined the metastable phase transitions of confined chain fluids. The phase transitions in a slit pore always take place at the lower pressure than the bulk saturation pressure. Also, capillary condensation/evaporation and layering transitions in the pore are contained within the gas-liquid equilibrium curves of the corresponding bulk fluid. As for the bulk systems, the critical temperatures for both metastable layering and capillary transitions increase with the chain length. The metastable layering transitions and capillary condensation/evaporation are represented by some sharp reductions of the grand potential. The intersections between the grand potential curves from adsorption and desorption processes allow us to determine the positions of the thermal equilibrium.

ACKNOWLEDGMENT

The research has been sponsored by the National Science Foundation (Grant Nos. CTS0406100 and CTS0340948).

- ¹D. N. Theodorou, in *Computer Simulations of Surfaces and Interfaces*, edited by B. Dunweg (Kluwer Academic, Netherlands, 2003), p. 329.
- ²T. J. Barton, L. M. Bull, W. G. Klemperer *et al.*, Chem. Mater. **11**, 2633 (1999).
- ³N. Maeda and J. N. Israelachvili, J. Phys. Chem. B **106**, 3534 (2002).
- ⁴L. D. Gelb, K. E. Gubbins, R. Radhakrishnan, and M. Sliwinski-Bartkowiak, Rep. Prog. Phys. **62**, 1573 (1999).
- ⁵K. Binder, Adv. Polym. Sci. **138**, 1 (1999).
- ⁶E. Kierlik, P. A. Monson, M. L. Rosinberg, and G. Tarjus, J. Phys.: Condens. Matter **14**, 9295 (2002).
- ⁷M. Muller, L. G. MacDowell, and A. Yethiraj, J. Chem. Phys. **118**, 2929 (2003).
- ⁸N. Maeda, M. M. Kohonen, and H. K. Christenson, Phys. Rev. E **61**, 7239 (2000).
- ⁹P. Bryk, K. Bucior, S. Sokolowski, and G. Zukocinski, J. Phys. Chem. B **109**, 2977 (2005).
- ¹⁰A. Maciolek, A. Drzewinski, and P. Bryk, J. Chem. Phys. **120**, 1921 (2004).
- ¹¹P. Bryk and S. Sokolowski, J. Chem. Phys. **121**, 11314 (2004).
- ¹²D. Chandler, J. D. McCoy, and S. J. Singer, J. Chem. Phys. **85**, 5971 (1986).
- ¹³C. E. Woodward, J. Chem. Phys. **94**, 3183 (1991).
- ¹⁴A. Yethiraj and C. E. Woodward, J. Chem. Phys. **102**, 5499 (1995).
- ¹⁵E. Kierlik and M. L. Rosinberg, J. Chem. Phys. **97**, 9222 (1992).
- ¹⁶Y. X. Yu and J. Z. Wu, J. Chem. Phys. **117**, 2368 (2002).
- ¹⁷Y. X. Yu and J. Z. Wu, J. Chem. Phys. **118**, 3835 (2003).
- ¹⁸D. P. Cao and J. Z. Wu, J. Chem. Phys. **121**, 4210 (2004).
- ¹⁹D. P. Cao and J. Z. Wu, Macromolecules **38**, 971 (2005).
- ²⁰Z. D. Li, D. Cao, and J. Z. Wu, J. Chem. Phys. **122**, 174708 (2005).
- ²¹Y. X. Yu, J. Z. Wu, F. Q. You, and G. H. Gao, Chin. Phys. Lett. **22**, 246 (2005).
- ²²N. Maeda, J. N. Israelachvili, and M. M. Kohonen, Proc. Natl. Acad. Sci. U.S.A. **100**, 803 (2003).
- ²³R. L. Cotterman, B. J. Schwarz, and J. M. Prausnitz, AIChE J. **32**, 1787 (1986).
- ²⁴W. A. Steele, J. Chem. Phys. **65**, 5256 (1976).
- ²⁵Y. P. Tang and J. Z. Wu, Phys. Rev. E **70**, 011201 (2004).
- ²⁶Y. X. Yu and J. Z. Wu, J. Chem. Phys. **117**, 10156 (2002).
- ²⁷R. Roth, R. Evans, A. Lang, and G. Kahl, J. Phys.: Condens. Matter **14**, 12063 (2002).
- ²⁸Y. Rosenfeld, Phys. Rev. Lett. **63**, 980 (1989).
- ²⁹J. K. Johnson, E. A. Muller, and K. E. Gubbins, J. Phys. Chem. **98**, 6413 (1994).
- ³⁰Y. P. Tang and J. Z. Wu, Phys. Rev. E **70**, 011201 (2004).
- ³¹W. G. Chapman, K. E. Gubbins, G. Jackson, and M. Radosz, Fluid Phase Equilib. **52**, 31 (1989).
- ³²J. Z. Wu and J. Prausnitz, Fluid Phase Equilib. **194**, 689 (2002).